

Design of NiTi-based shape memory microcomposites with enhanced elastocaloric performance by a fully thermomechanical coupled phase-field model



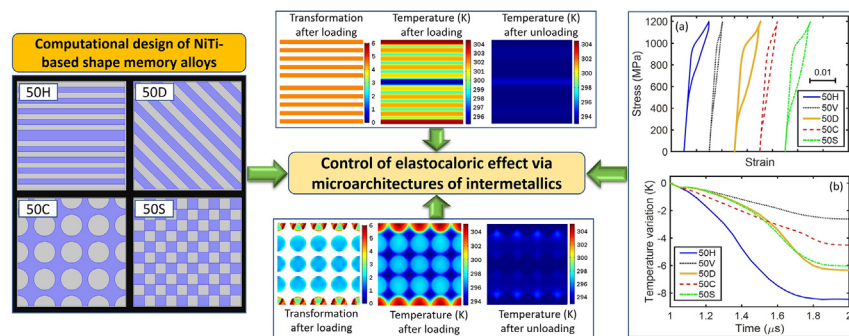
Cheikh Cissé, Mohsen Asle Zaeem*

Department of Mechanical Engineering, Colorado School of Mines, 1500 Illinois street, Golden, CO 80401, USA

HIGHLIGHTS

- Effect of intermetallics on the elastocaloric effect (eCE) of NiTi is studied.
- Microcomposites consisting of NiTi and intermetallic phases are designed by phase-field modeling.
- Highest hitherto reported coefficient of performance (COP) of 67.13 is achieved.
- Higher intermetallic volume fraction ensures higher COP but lower temperature change.
- Finer aspect ratio of the intermetallic phase induces higher eCE.

GRAPHICAL ABSTRACT



ARTICLE INFO

Article history:

Received 29 April 2021

Revised 25 May 2021

Accepted 9 June 2021

Available online 10 June 2021

Keywords:

Elastocaloric effect
Shape memory alloy
Microcomposite
Phase-field modeling

ABSTRACT

The non-transforming intermetallic Ni_3Ti phase generated in NiTi matrix by additive manufacturing was previously reported to create elastocaloric composites with a great coefficient of performance (COP) between 11 and 22 [Hou et al., *Science* 366 (6469) (2019) 1116–1121]. In this work, we use a fully thermomechanical coupled phase-field model to design microarchitectures considering the effects of all the possible non-transforming intermetallics (Ni_4Ti_3 , Ni_3Ti , and Ti_2Ni) in NiTi. Our simulations show possibilities of increasing the COP by guiding the type, shape and volume fraction of intermetallics, which are controllable by processing parameters. With 50% intermetallic fraction arranged in strips of 500 nm width perpendicular to the loading direction, the Ti_2Ni intermetallic induces higher COP (67.13) than Ni_3Ti (16.18) and Ni_4Ti_3 (14.29), all surpassing that of the bulk NiTi without intermetallics (12.92). Additionally, the COP increases to 79.94 for 65% volume fraction of Ti_2Ni and decreases to 56.31 for 35% Ti_2Ni content. Even nontrivial designs with 50% of circular or square transforming NiTi domains display high COP of 40.06 and 29.22, respectively. A high COP is achievable by introducing intermetallics having high modulus (for low input energy), thermal conductivity (for temperature change) and heat capacity (for the output energy).

© 2021 The Author(s). Published by Elsevier Ltd. This is an open access article under the CC BY-NC-ND license (<http://creativecommons.org/licenses/by-nc-nd/4.0/>).

1. Introduction

Shape memory alloys (SMAs) have several actuation-based applications in aerospace, automotive, biomedical, and civil engineering [1–6], most of which are mediated by the unique shape

* Corresponding author.

E-mail address: zaeem@mines.edu (M. Asle Zaeem).

recovery via reversible austenite–martensite phase transformations. Aside from the mechanical features of the martensitic phase transformation, its large recoverable inelastic deformation generates important entropy changes. The inherent heat release (exothermic) and heat absorption (endothermic) during, respectively, the forward austenite-to-martensite and reverse martensite-to-austenite transformation [7,8] have stimulated interest for thermal management applications. Especially, the heat consumption during pseudoelastic martensite-to-austenite transformation [9–12] appears as a unique way to develop solid-state elastocaloric cooling technologies that are green alternatives to vapor compression cooling processes damaging the climate [13–19]. In recent years, several researchers have studied the thermograms of SMAs [20–22], especially for NiTi [17,23], leading to device prototyping and fabrication such as miniature heat pumps [24]. The Brayton cycle illustrated in Fig. 1 corresponds to the simplest case for elastocaloric effect (eCE) with four-stages, namely an adiabatic pseudoelastic loading (stage 1), the transfer of the released heat to a sink (stage 2), an adiabatic pseudoelastic unloading (stage 3), and the absorption of heat from a source corresponding to the cooling effect (stage 4).

Several experimental approaches have been tested to develop eCE devices [9,29,30], most of which use NiTi wires and ribbons [26], NiTi films and foils [24,27,31–35], NiTi plates and sheets [33,36] or NiTi tubes [37,38]. In particular, the films and foils are advantageous in small scale applications [21,39–41]. For device development, the heat transfer capability of the material is more important than other features [9]. In term of latent heat and energy conversion, NiTi under compression [17,42,43], TiNiCu under tension [22,25,34], and CuZnAl [44], CuAlMn [45] and CuAlBe [46] under tension are the most promising elastocaloric SMAs. Among these materials, NiTi is the most interesting one due to a latent heat as high as 35 J/g [47], a large adiabatic temperature variation up to 31.5 K [43,48,49], and an isothermal entropy variation up to 70.7 J.Kg⁻¹.K⁻¹ [12].

A perfect eCE material needs to have a small mechanical hysteresis (input energy), a low critical transformation stress, a very high temperature variation (output energy), and a sustainable fatigue life (durability). In a recent work, using Laser Directed Energy Deposition (L-DED) we additively manufactured an exceptionally

stable and efficient eCE material with complex nanostructured composites. This material consisted of NiTi matrix and Ni₃Ti intermetallic phases with nearly 50% volume fraction of each (Fig. 2a). The coefficient of performance (COP), measuring the cooling efficiency as the ratio of the output to input energies of a pseudoelastic cycle [50,51], was between 11 and 22, which is consistent with the value of 17.7 reported for NiTi made by Laser Engineered Net Shaping (LENS) [52], and higher than the COP of the as-casted NiTi between 4.4 [17] and 11.8 [52]. In general, depending on the composition of the powder, (Ni-rich or Ti-rich) and the fabrication procedure and its parameters, the intermetallic phase can be either Ni₄Ti₃ [17,53,54], Ni₃Ti [17,54], or Ti₂Ni [17,52,54–56]. Also, the intermetallic phase can adopt linear fiber-like or dendritic-like [17,54,56], flake-like [52,54], particle-like [52,54], grain boundary-like [54], or whisker-like [54] shapes (see Fig. 2). Often only one intermetallic phase emerges, but in the case of whisker-like both Ni₄Ti₃ and Ni₃Ti appeared [54].

Experimental studies showed that, depending on the intermetallic type, the average thermal conductivity of the NiTi-based composite can change drastically [57]. This entails that the eCE can be affected by features such as the volume fraction, orientation, composition, and distribution of such intermetallic phases. In the present context of additive manufacturing, we can optimize elastocaloric cooling by processing desirable topology into material components. To remedy the time and cost limitations of experimental methods, we will use quantitative phase-field modeling (PFM) to study the eCE of NiTi and design SMA composites with improved COP.

Only a few modeling works were dedicated to study the eCE of SMAs. Lumped element models (LEM) were used by Bruederlin et al. [27] to predict 13 K temperature drop during cooling of NiTi foils and films, and by Ossmer et al. [24] to model the eCE in a miniature-scale heat pumping device. Other researchers adopted Tanaka-type phenomenological models to assess the eCE of CuAlZn and NiTi [51,58], macroscopic models to study the eCE in NiTi tube [59] or analytical models mimicking electrical low pass filter to study cascade caloric refrigeration systems [60]. Wendler et al. [50] proposed one of the rare PFMs for predicting the temperature profile in NiTi films. However, their model considered a piecewise free energy function. More recently, Qian et al. [61–63] used a 1D

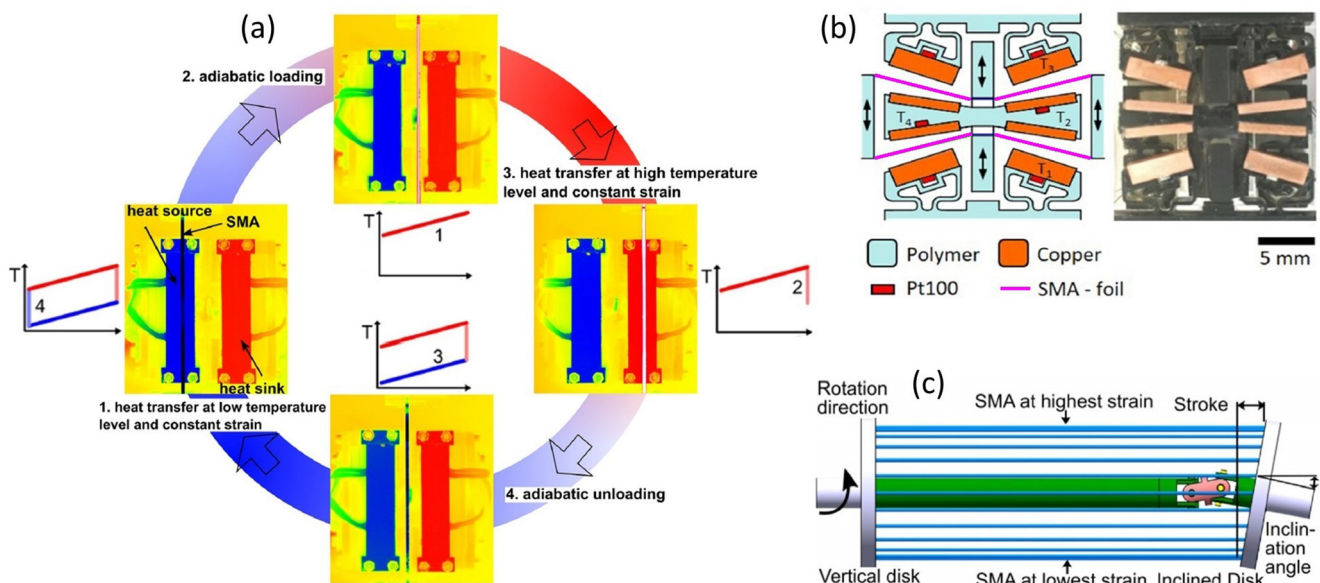


Fig. 1. (a) Schematic Brayton eCE operation cycle, adapted from [25] and [26], (b) SMA foil-based elastocaloric prototype [24,27], and (c) SMA wire-based elastocaloric device [28].

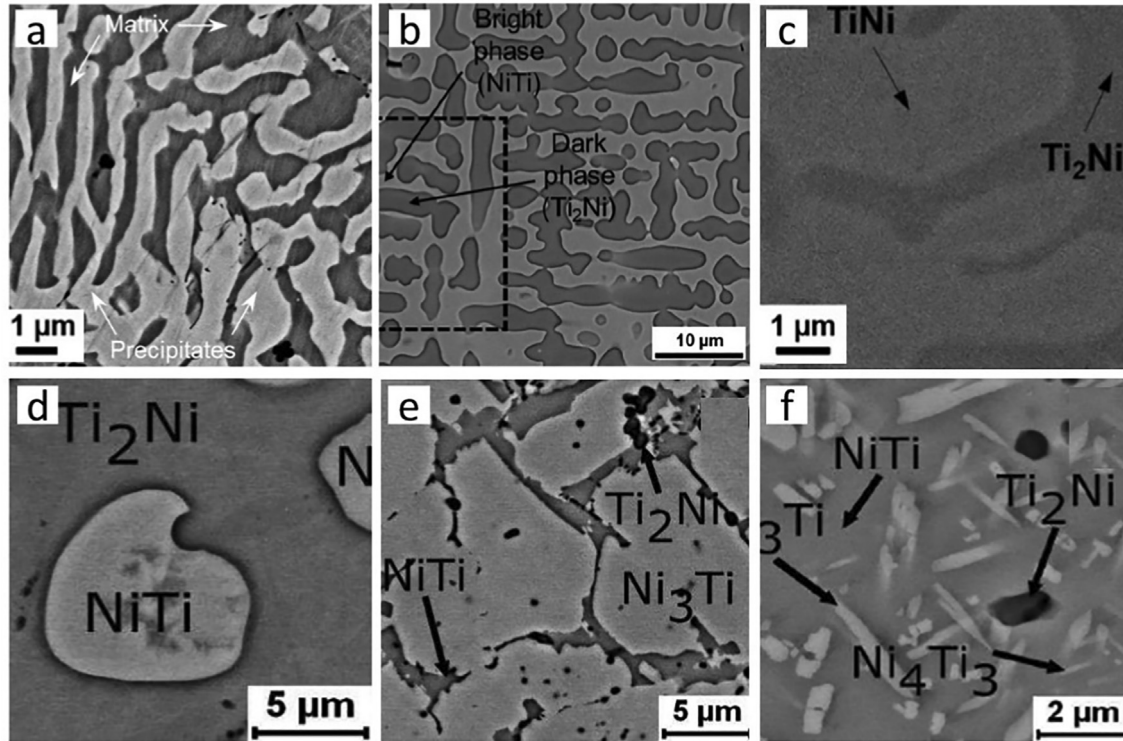


Fig. 2. Different microcomposites with: (a) dendritic-like Ni_3Ti [17], (b) dendritic-like Ti_2Ni [56], (c) flake-like Ti_2Ni [52], (d) particle-like Ti_2Ni [54], (e) grain boundary-like NiTi [54], and (f) whisker-like Ni_4Ti_3 and Ni_3Ti [54].

transformation kinetic model to investigate the pseudoelastic thermal in SMAs. Landau-like PFMs helped evaluate the strain rate sensitivity [64,65] and the dynamic and quasiplastic responses [66,67] of NiTi . All these models consider either homogeneous, macroscopic, single phase materials or use constant model and materials parameters and are not thermomechanically coupled. Recently, we developed a fully thermomechanically coupled PFM [46] for a pioneering eCE study in polycrystalline CuAlBe , considering the effect of loading rates and plasticity and functional fatigue.

In this work, we will advance our start-of-the-art PFM [46] to include transforming and non-transforming phases and design NiTi -based eCE microcomposites with enhanced eCE. The PFM is fully thermomechanically coupled using temperature-dependent energy coefficients and a transformation-dependent heat diffusion equation. The model is also advanced by considering six martensite variants. The transformation governing equations are assigned only to the transforming domains, while the heat and mechanical governing equations are assigned to both transforming and non-transforming domains. The paper is architected as follows: the PFM and governing equations are derived in Section 2, the simulation results are given and discussed in Section 3, and conclusions and perspectives are provided in Section 4.

2. Thermomechanical coupled Phase-Field model

The state variables or order parameters (OPs) of the PFM used to track the phase transformation and denoted by η_ν for the ν^{th} martensite variant. When $\eta_\nu = 1$ the SMA is its purely martensitic as the ν^{th} variant, while $\eta_\nu = 0$ describes either a pure austenitic phase or a mix of austenite and other martensite variants. Considered as a closed thermodynamic system, the SMA can be fully described by a potential corresponding to a total free energy F . It is composed by the chemical or bulk free energy (F_{bk}) describing the basic transformation of the material, the gradient free energy

(F_{gd}) describing the interface properties, the classic thermal free energy (F_{th}), and the elastic free energy (F_{el}).

2.1. Bulk energy

The bulk free energy drives the microstructure evolution under the sole temperature variation. It is given by the following 2–4–6 polynomial function of the OPs [68,69]:

$$F_{ch}(\eta_p, T) = \int \left[\frac{A_1(T)}{2} \sum_{\nu=1}^N \eta_\nu^2 - \frac{A_2(T)}{4} \sum_{\nu=1}^N \eta_\nu^4 + \frac{A_3(T)}{6} \left(\sum_{\nu=1}^N \eta_\nu^2 \right)^3 \right] dV, \quad (1)$$

where N is the number of martensite variants. The coefficients $A_1(T)$, $A_2(T)$ and $A_3(T)$ are positive continuous functions of temperature and are related to the energy gap between austenite and martensite, $\Delta F(T)$, as follows,

$$\begin{cases} A_2(T) = 4A_1(T) - 12\Delta F, \\ A_3(T) = 3A_1(T) - 12\Delta F, \\ \Delta F(T) = Q(T/T_0 - 1). \end{cases} \quad (2)$$

where Q is the latent heat, and T_0 is the equilibrium temperature. The thermomechanical coupling is enforced by defining the following continuous function of temperature defined for coefficient $A_1(T)$:

$$A_1(T) = \begin{cases} Q \exp \left[m_1 \left(\frac{T-T_0}{T_0} \right) \right], & \text{for } T \leq T_0 \\ Q \exp \left[m_2 \left(\frac{T-T_0}{T_0} \right) \right], & \text{for } T > T_0 \end{cases}, \quad (3)$$

where m_1 and m_2 are positive constants.

2.2. Gradient energy

The gradient free energy ensures that the phase transition is smooth across the interfaces between the different phases. When considered isotropic, it has a simple expression that reads

$$F_{gd}(\eta_1, \eta_2, \dots, \eta_m) = \frac{1}{2} \int \beta \sum_{v=1}^N (\nabla \eta_v)^2, \quad (4)$$

where coefficient β is related to the interface thickness and ∇ is the gradient operator.

2.3. Thermal energy

The classic expression of the thermal energy reads [70]:

$$F_{th}(T) = C_p \left[(T - T_0) - T \ln \left(\frac{T}{T_0} \right) \right], \quad (5)$$

where C_p is the heat capacity at constant pressure of the material assumed the same for both martensite and austenite.

2.4. Elastic energy

This energy term is generated in the system to accommodate the microstructural changes. It is expressed as

$$\begin{aligned} F_{el}(\boldsymbol{\varepsilon}, \eta_v) &= \frac{1}{2} \int \boldsymbol{\varepsilon}^{el} : \mathbf{K}(\eta_v) : \boldsymbol{\varepsilon}^{el} dV \\ &= \frac{1}{2} \int (\boldsymbol{\varepsilon} - \boldsymbol{\varepsilon}^{tr}) : \mathbf{K}(\eta_v) : (\boldsymbol{\varepsilon} - \boldsymbol{\varepsilon}^{tr}) dV, \end{aligned} \quad (6)$$

in which $\boldsymbol{\varepsilon}^{el}$, $\boldsymbol{\varepsilon}^{tr}$ and $\boldsymbol{\varepsilon}$ are respectively the elastic, transformation and total strain tensors. The inhomogeneous elasticity is taken into account via the following equivalent stiffness tensor $\mathbf{K}(\eta_v)$ as a OP-dependent function given by [70,71]:

$$\mathbf{K}(\eta_v) = \mathbf{K}^A + \left| \sum_{v=1}^m \eta_v \right| (\mathbf{K}^M - \mathbf{K}^A), \quad (7)$$

where \mathbf{K}^A is the stiffness tensors of austenite and \mathbf{K}^M is that of martensite. The transformation strain $\boldsymbol{\varepsilon}^{tr}$ is defined as a function of the Bain strain tensors $\boldsymbol{\varepsilon}_v^{00}$ of the variants by [70,71]:

$$\boldsymbol{\varepsilon}^{tr} = \sum_{v=1}^N \eta_v^2 \boldsymbol{\varepsilon}_v^{00}. \quad (8)$$

Contrary to most of the existing PFMs that consider only two martensite variants for plane strain problems [65,66], we will use all the available (six) NiTi martensite variants that remain in a two-dimensional (2D) domain with the following eigen strain tensors [72,73]:

$$\begin{aligned} \boldsymbol{\varepsilon}_1^{00} &= \begin{pmatrix} \theta & \gamma \\ \gamma & \alpha \end{pmatrix}, \boldsymbol{\varepsilon}_2^{00} = \begin{pmatrix} \theta & -\gamma \\ -\gamma & \alpha \end{pmatrix}, \boldsymbol{\varepsilon}_3^{00} = \begin{pmatrix} \alpha & \gamma \\ \gamma & \theta \end{pmatrix} \\ \boldsymbol{\varepsilon}_4^{00} &= \begin{pmatrix} \alpha & -\gamma \\ -\gamma & \theta \end{pmatrix}, \boldsymbol{\varepsilon}_5^{00} = \begin{pmatrix} \alpha & \tau \\ \tau & \alpha \end{pmatrix}, \boldsymbol{\varepsilon}_6^{00} = \begin{pmatrix} \alpha & -\tau \\ -\tau & \alpha \end{pmatrix} \end{aligned} \quad (9)$$

with $\alpha = 0.0243$, $\theta = -0.0437$, $\gamma = -0.0427$, $\tau = 0.058$.

2.5. Governing equations

2.5.1. Evolution of order parameters

The time and space evolutions of the OPs are obtained by solving by the Ginzburg-Landau governing equation [74,75]:

$$\frac{\partial \eta_v}{\partial t} = -M \frac{\partial F}{\partial \eta_v}, \quad (10)$$

where the kinetic coefficient M describes the interface mobility.

2.5.2. Thermal distribution and evolution

The heat absorption or release during the adiabatic austenite-to-martensite induce temperature variation in the material. The distribution and evolution of the temperature are obtained from the heat equation:

$$\rho C_p \frac{\partial T}{\partial t} = k \nabla^2 T + \sum_{v=1}^N Q \dot{\eta}_v, \quad (11)$$

where ρ is the mass density, and k is the thermal conductivity.

2.5.3. Mechanical equilibrium equations

We apply a surface force (\mathbf{t}^a) on the boundary portion (S_t) and a displacement field (\mathbf{u}^a) on the boundary portion (S_u) of a 2D solid domain (S). The mechanical equilibrium is expressed as

$$\begin{cases} \nabla \boldsymbol{\sigma} = \mathbf{0} & \text{in } \Omega \\ \boldsymbol{\sigma} \cdot \mathbf{n} = \mathbf{t}^a & \text{on } \Omega_t, \\ \mathbf{u} = \mathbf{u}^a & \text{on } \Omega_u \end{cases} \quad (12)$$

where $\boldsymbol{\sigma}$ is the Cauchy stress.

2.6. Details of numerical simulations and material properties

The nonlinear governing equations are solved by the mathematics module of COMSOL Multiphysics using the ‘‘Fully Coupled’’ approach so that convergence is obtained with less iterations compared to the ‘‘Segregated’’ method. We used the MUMPS ‘‘Direct’’ algorithm solver which gives a more robust solution and is preferred to the ‘‘Iterative’’ solver that is sensitive to the geometric and material gradients. Depending on the regularity of the geometry, we use either mapped quadratic elements with size of 50 nm, or free quadratic triangular mesh with element size between 50 nm and 100 nm. The governing equations are solved using the material parameters given in Tables 1 for the NiTi matrix and Table 2 for the intermetallic phases. The parameter m_2 is adjusted so that the critical stress for martensitic transformation of the bulk sample is comparable to experimental data in [76].

3. Results and discussions

We investigate the eCE of the microcomposites both in terms of the temperature variation, especially during the unloading stage, and the COP, for the specimens shown in Fig. 3. The samples are subjected, at room temperature, to a maximum compressive load of 1200 MPa during a ramp of 1 μ s before unloading to 0 MPa during another ramp of 1 μ s (see Fig. 3(a)). The specimen in Fig. 3(b) is used as the reference and compared to the others. The SMA matrix uses the properties of a polycrystal with random grain orientations.

Table 1
NiTi material parameters.

Parameter	Value
Latent heat Q (MJ.m ⁻³)	38.06 [17]
Kinetic coefficient M (m ³ .J ⁻¹ .s ⁻¹)	0.5 [77]
Equilibrium temperature T_0 (K)	253 [17,78]
Austenite elastic modulus E_A (GPa)	92 [79]
Martensite elastic modulus E_M (GPa)	72 [79]
Poisson ratio ν (-)	0.3 [79]
Gradient energy coefficient β (J.m ⁻¹)	1x10 ⁻¹⁰ [77]
Energy coefficient parameter m_2	1 [76]
density ρ (kg.m ³)	6450 [80]
Thermal conductivity k (W.m ⁻¹ .K ⁻¹)	10 [80]
Heat capacity C_p (J.kg ⁻¹ .K ⁻¹)	550 [43]
Domain size (μ m ²)	10 × 10

Table 2
Material parameters for the intermetallics.

Parameter	Ni ₄ Ti ₃	Ni ₃ Ti	Ti ₂ Ni
Elastic constant C_{11} (GPa)	218 [81]	345 [82]	228.2 [83]
Elastic constant C_{33} (GPa)	255 [81]	345 [82]	228.2 [83]
Elastic constant C_{13} (GPa)	125 [81]	122 [82]	105 [83]
Elastic constant C_{44} (GPa)	36 [81]	87 [82]	42.6 [83]
Mass density ρ (kg.m ³)	6770 [84]	7950 [84]	5640 [84]
Thermal conductivity λ (W.m ⁻¹ .K ⁻¹)	16.5 [85]	30 [85]	7 [86]
Specific heat C_p (J.kg ⁻¹ .K ⁻¹)	345 [87]	380 [87]	3452.6 [83]

3.1. Influence of different intermetallic phases on elastocaloric effect

We first study the eCE of the 50H with 10 intermetallic strips perpendicular to the loading direction; each strip has a 500 nm width. Fig. 4(a) compares the pseudoelastic curves of the microcomposite for different intermetallic phases to the bulk SMA (without intermetallic phase). The effective moduli of the microcomposite are higher than the typical austenite, which indicates the mechanical effect of non-transforming intermetallic phases. The transformation starts at around 950 MPa for bulk NiTi and at 800 MPa for 50H. These values are obtained by using the average stress in the sample at the same time reference where the sum of the order parameters reaches 0.002 (similar to the 0.2% proof stress for elastoplastic materials). This lower transformation stress in 50H is due to the constraints exerted by the intermetallic phases. The smaller hysteresis loop than the bulk SMA is due to the elastic deformation of the intermetallic phase during the whole pseudoelastic cycle. The size of the closed envelop corresponds to the input energy and is 2.743 MJ.m⁻³ for the bulk NiTi, and 1.303 MJ.m⁻³, 1.304 MJ.m⁻³ and 1.436 MJ.m⁻³ for 50H with Ni₄Ti₃, Ni₃Ti, and Ti₂Ni intermetallic phases, respectively. The evolution of the average temperature variations (ΔT) during unloading, defined as the difference between the current average temperature and the end-of-loading average temperature is shown in Fig. 4(b). The maximum absolute ΔT is 16.86 K for the bulk SMA, against 8.17 K, 8.07 K and 8.15 K for 50H with respectively, Ni₄Ti₃, Ni₃Ti, and Ti₂Ni secondary phases. The COP of the microcomposite is calculated as [50,51]:

$$\text{COP} = \frac{\Delta W_T}{\Delta W_m} = \frac{\rho \cdot |\Delta T| \cdot C_p}{\int \sigma \cdot d\varepsilon} \quad (13)$$

For the composites, we define the equivalent density and heat capacity as the volume averaged functions:

$$\rho = (1 - x_i)\rho_m + x_i\rho_i, \quad (14)$$

$$C_p = (1 - x_i)C_p^m + x_iC_p^i, \quad (15)$$

where subscripts “m” and “i” refer to, respectively, the matrix and the intermetallic of volume fraction x_i . The COP reads 12.92 for the bulk SMA, and 14.29, 16.18 and 67.13 for 50H with Ni₄Ti₃, Ni₃Ti, and Ti₂Ni intermetallic phases, respectively. The computational COP obtained with Ni₃Ti intermetallic is consistent with those of the experimental L-DED (between 11 and 22) and the value of 17.7 of LENS [52]. The temperature variation of 8.07 K is also agrees well with the experimental data of between 4.1 K for L-DED [17] and 7.5 K for LENS [52]. When using the Ti₂Ni intermetallic, the temperature variation remains in the same range (8.15 K). However, the very high specific heat capacity of the Ti₂Ni intermetallic generates an excellent COP that is four times higher than those of Ni₄Ti₃, nearly five times that of Ni₃Ti, and three times the maximum experimentally reported value of 22. Therefore, we advise to control the additive manufacturing process to generate this intermetallic rather than others.

To understand the origins of this phenomenon, we compare in Fig. 5 the change in microstructure after loading (top row) and unloading (second row) to the temperature variation at after loading (third row) and unloading (bottom row) during the pseudoelastic cycle of Fig. 4(a). It can be noticed that the increase (decrease) of temperature in the materials correlates well with the degree of forward (reverse) transformation. In absence of secondary phase, the bulk SMA displays homogeneous transformation and temperature, in contrast to the microcomposites where temperature minima values are spotted in the horizontal central axis. The changes in thermomechanical properties explain the difference in the values of the local temperature minima between the specimens, even if the local temperature maxima are very close. Another noticeable

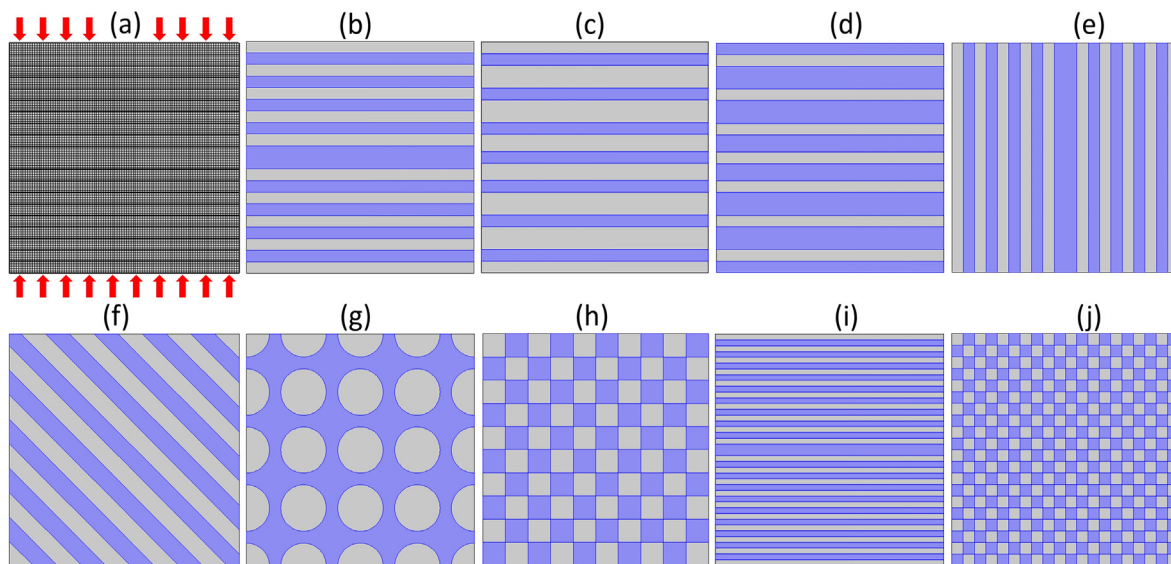


Fig. 3. (a) meshed sample under compressive load, (b) reference sample with 50% of intermetallic horizontal strips (50H), (c) 35% horizontal strips (35H), (d) 65% horizontal strips (65H), (e) 50% vertical strips (50V), (f) 50% diagonal strips (50D), (g) 50% circular transforming particles (50C), (h) 50% coarse square particles (50S), (i) 50% fine strips (50H2), (j) 50% fine square particles (50S2). The matrix is in grey and the intermetallic in blue. (For interpretation of the references to colour in this figure legend, the reader is referred to the web version of this article.)

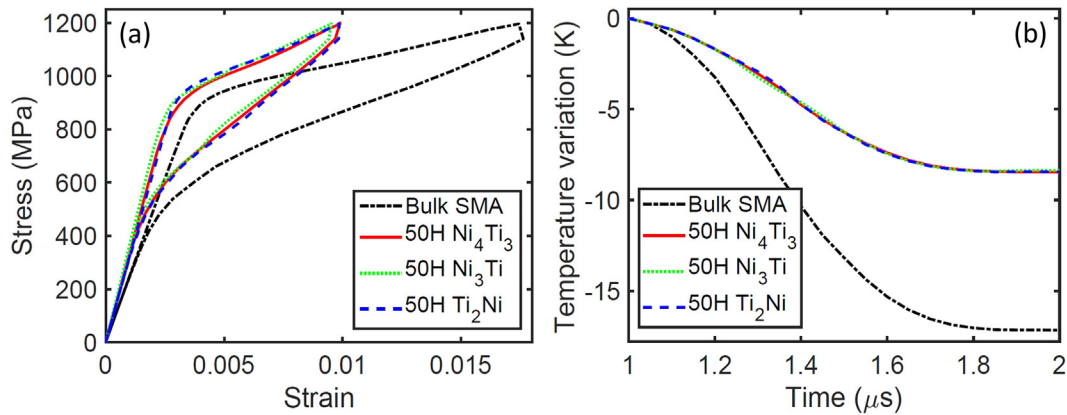


Fig. 4. (a) Pseudoelastic responses at initial room temperature, and (b) the unloading average temperature of the bulk NiTi (dotted black curve) and 50HS (colored curves).

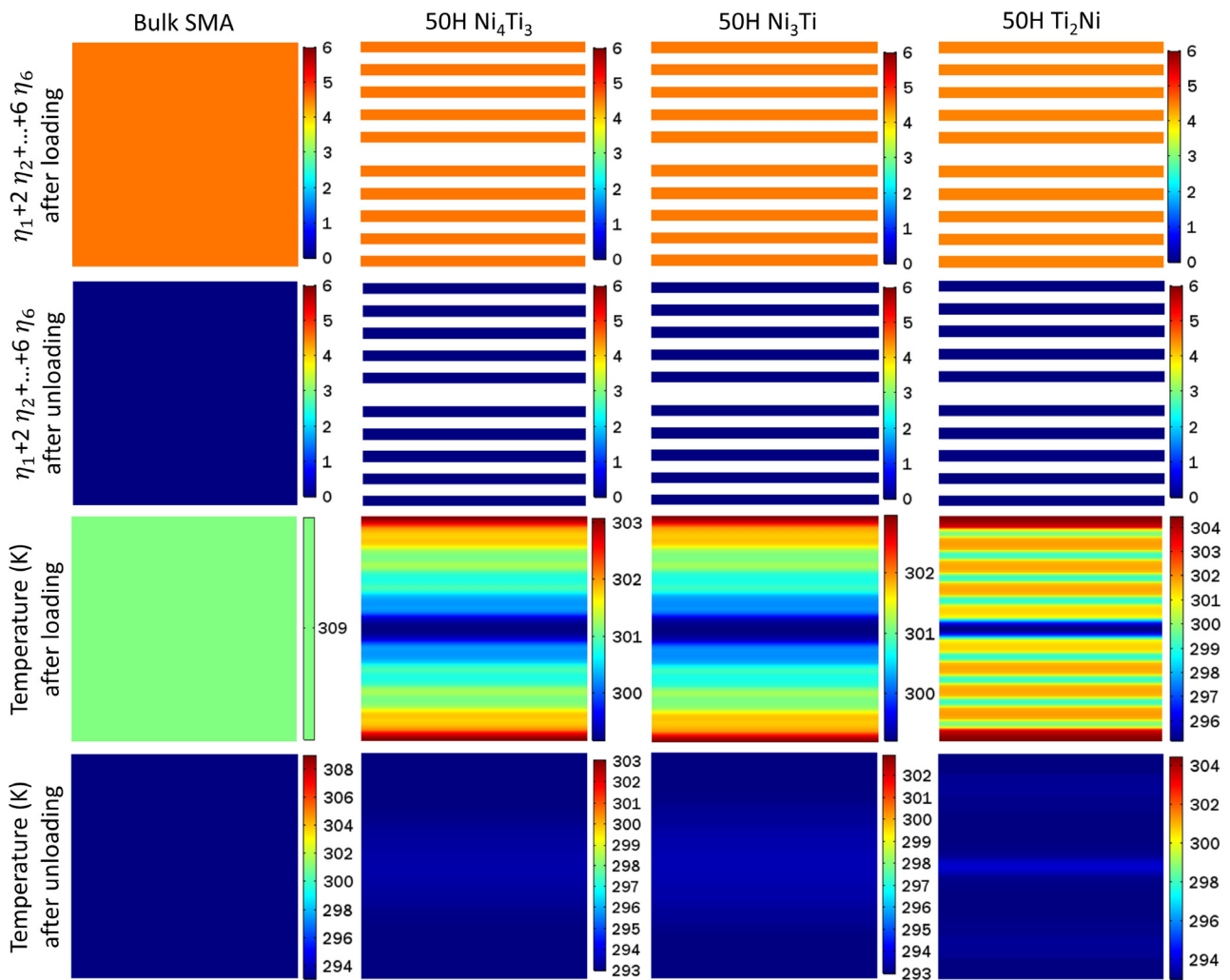


Fig. 5. Evolution of the martensite distribution (top and second rows) where 0 in the legend corresponds to the austenite and the other integers are for the martensite variants; local temperature distribution (third and bottom rows) of the in the bulk SMA (left column) and 50H microcomposites with Ni₄Ti₃ (second column), Ni₃Ti (third column) and Ti₂Ni (fourth column) during the pseudoelastic cycle.

remark is the difference in temperature gradient between the samples despite their very close average temperature variation Fig. 4 (b), which we attribute to the thermal parameters. Based on these results the remaining simulations will be conducted with Ti₂Ni intermetallic phase.

3.2. Effect of volume fraction of Ti₂Ni intermetallics on elastocaloric effect

To broaden our insights in the role of the intermetallic on the overall eCE of the microcomposites, this section studies the effect

of its volume fraction. To this end, we investigate two additional specimens, 35H and 65H, with 35% and 65% Ti_2Ni , respectively. Fig. 6(a) shows that as the proportion of intermetallic increases, the critical transformation stress decreases and the hysteresis loop decreases due to the lower quantity of transforming material, which in turn, results in steeper stress–strain curves. Such behavior is due to mechanical constraints of the non-transforming intermetallic phases and their load transfer with the transforming non-load-bearing matrix. Therefore, as the volume fraction of Ti_2Ni increases, the maximum average temperature variation in Fig. 6 (b) decreases. The respective COPs of 56.31, 67.13 and 79.94 are obtained for 35H, 50H and 65H, with average temperature variations of -10.7 K, -8.15 K, and -5.55 K. These results identify that, while a higher volume fraction for intermetallic phases provides a lower average temperature variation, its inherent smaller hysteresis guarantees a higher COP. However, the primary use of eCE is its heat absorption, which means that the amount of intermetallic phase should be limited to a critical value depending on the elastocaloric objective function. These results also demonstrate two crucial roles of the intermetallic phases consisting of (i) bear/transfer the mechanical load and (ii) redistribute/transfer the heat inside the microcomposite material.

The local distribution of martensite after loading (first column) and unloading (second column), and temperature after loading (third column) and unloading (fourth column) given by the inset in Fig. 6 help understanding the quantitative results. Depending on the geometric disposition of the strips, the horizontal central axis is where the local maximum temperature (65H) or the local

minimum temperature (35H and 50H) occurs after loading. It can be noticed that the local temperature maxima and minima are shifted up as the intermetallic content decreases, which correlates well with the two aforementioned roles of the secondary phase.

3.3. Effect of nanoarchitecture on elastocaloric effect

We used the PFM to design different microcomposites with various types of intermetallic nanoarchitecture, which would be expensive and time-consuming to do by experiments. In addition to the 50H specimen, we consider the 50V, 50D, 50C and 50S samples, shown in Fig. 3. In Fig. 7, for the same volume fraction of Ti_2Ni intermetallic, 50V with strips parallel to the loading direction yields to the lowest hysteresis loop corresponding to a quasilinear stress–strain curve. Such a lower degree of transformation explains its lowest temperature variation. When the strips are arranged diagonally, the response of 50D is between those of 50HS and 50VS, both for the pseudoelastic stress–strain curve and average temperature variation. With their nonlinear internal structures, 50S displays thermomechanical responses that are very close to 50D, while 50C stands alone compared to the remaining samples and tends to display a quasilinear mechanical response. The average temperature variations (and COP) for these samples during unloading are -2.32 K (43.75) for 50V, -6.03 K (27.32) for 50D, -4.212 K (40.06) for 50C, and -5.73 K (29.22) for 50S. This means that, depending on the prescribed minimum temperature variation, different eCE performance can be attained, all having a greater COP than the bulk SMA.

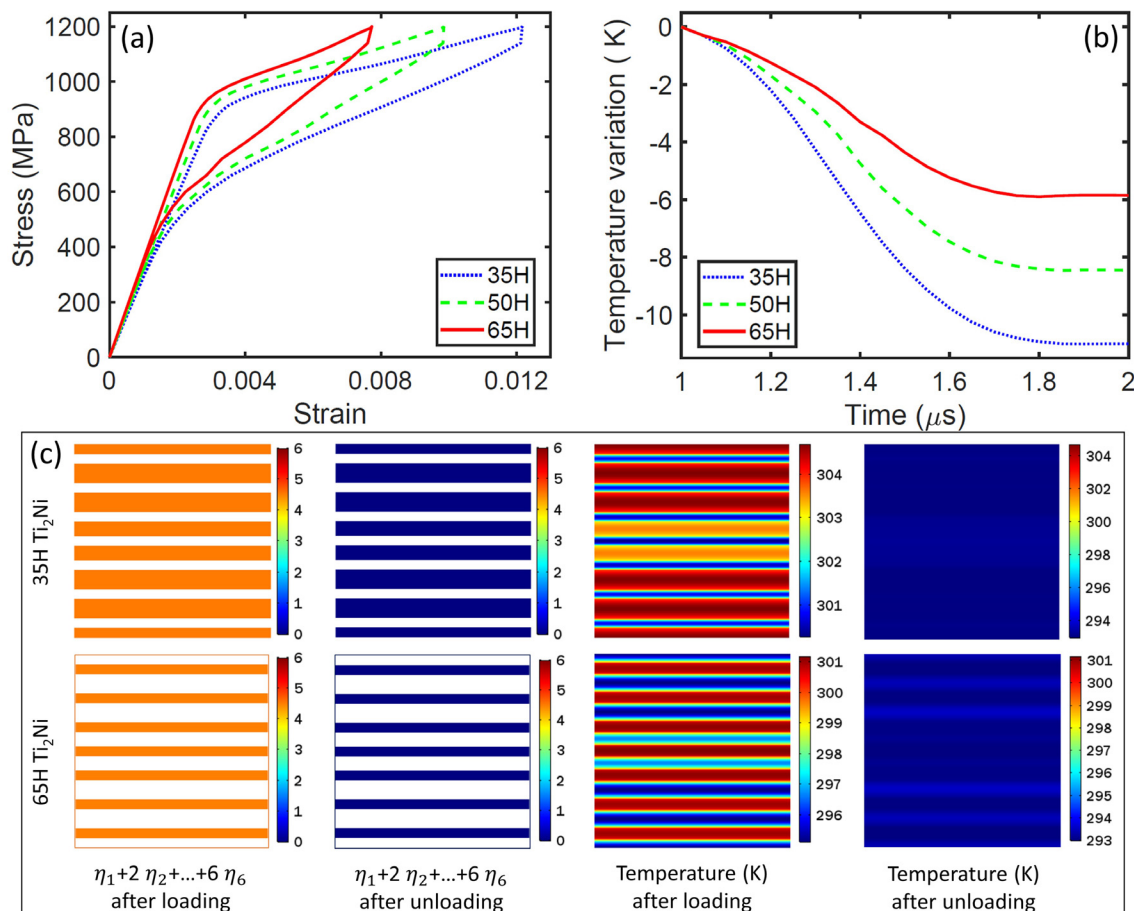


Fig. 6. (a) Pseudoelastic responses at room temperature, and (b) average temperature variation during unloading for different volume fraction of Ti_2Ni intermetallic phase. The insets give the martensite and temperature distribution during the pseudoelastic cycle.

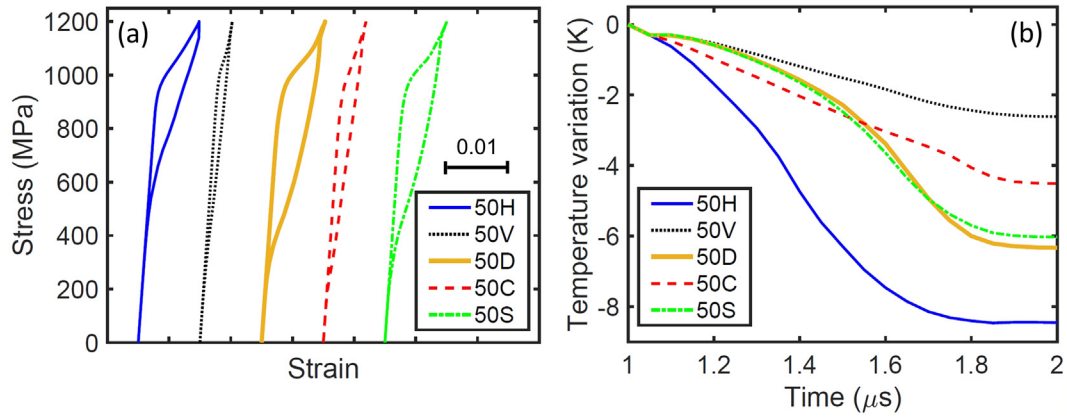


Fig. 7. (a) Pseudoelastic curves and (b) average temperature variation for different designs of microcomposites.

Fig. 8 shows heterogeneous distribution of the martensite phase and nonlinear gradient of the temperature inside the samples with 50 V and 50C display more transformation localization, contrary to 50H. This explains the neat difference in the average temperature variation in Fig. 7(b), despite very similar local maxima and mini-

mum in the samples. It can be also seen that a larger untransformed zone results in a lower minimum local temperature after loading. The bottom row in Fig. 8 is a demonstration of the eCE of the microcomposite in that the high (low) temperature zones after loading becomes the low (high) temperature areas after unloading.

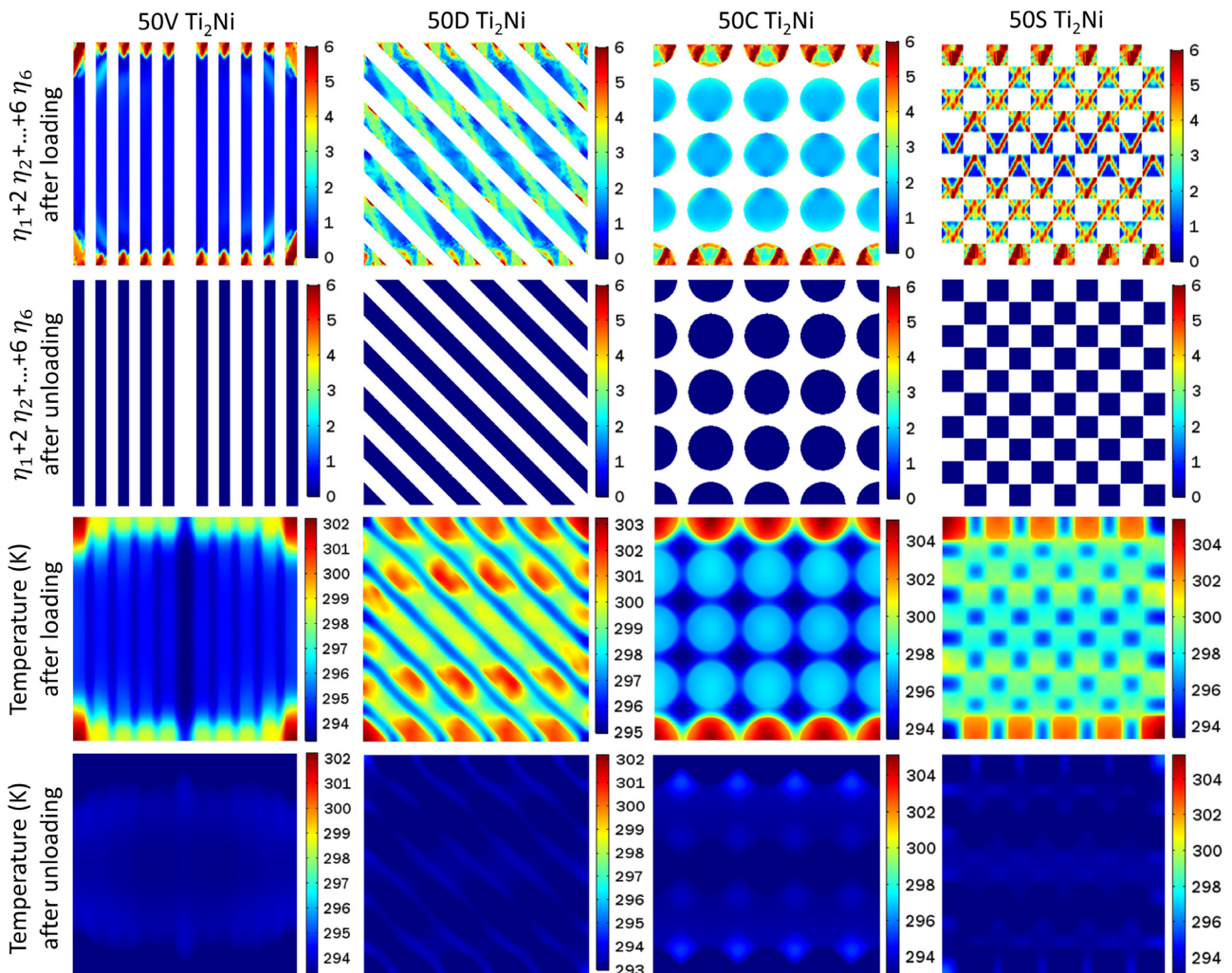


Fig. 8. Martensite distribution after loading (top row) and unloading (second row), and local distribution of temperature after loading (third row) and unloading (bottom row) for various microcomposite designs.

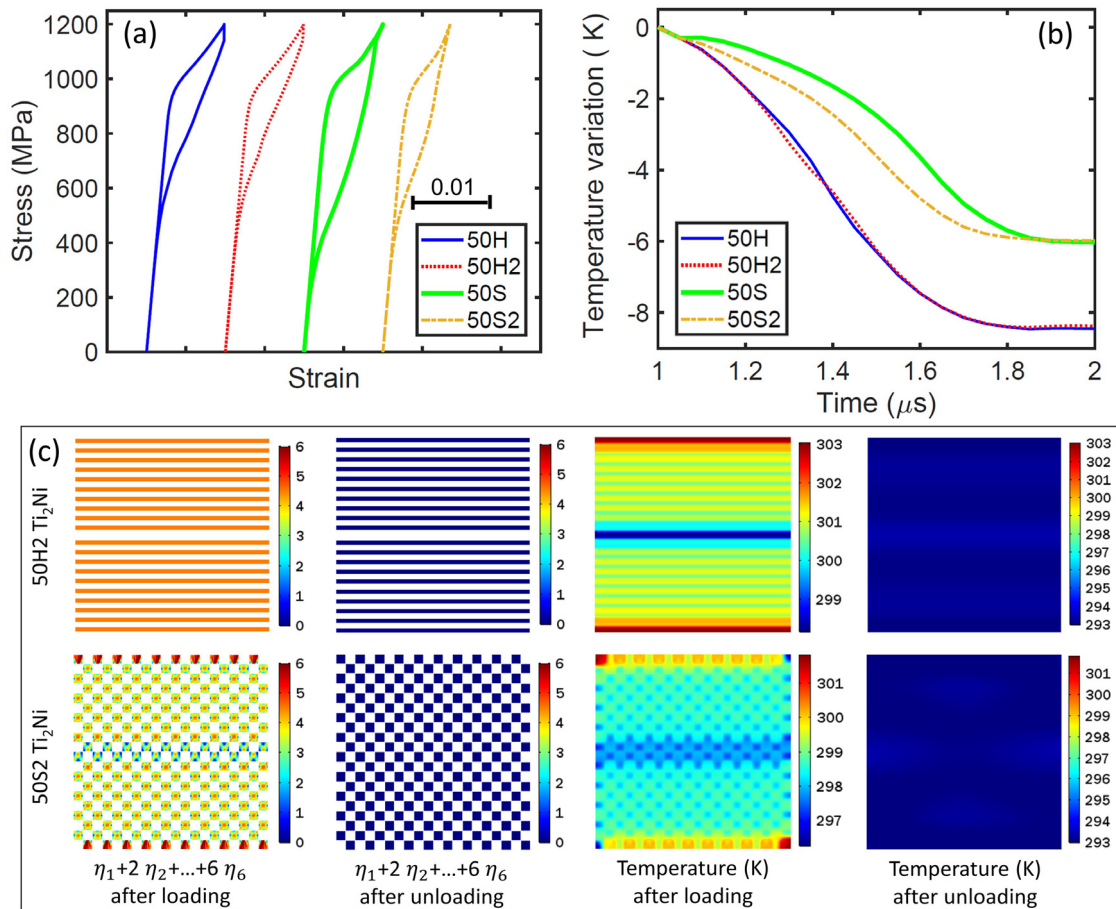


Fig. 9. (a) Pseudoelastic curves, and (b) average temperature variation of the microcomposites for different aspect ratios of the intermetallic phase. The insets give the martensite and temperature distributions during the pseudoelastic cycle for various smaller aspect ratios of the intermetallic.

3.4. Effect of aspect ratio of intermetallic on elastocaloric effect

We study another feature of the microcomposites which is the aspect ratio of the intermetallic phase. To this end, we consider additional samples, namely 50H2 with 250 nm strip width against 500 nm for 50H, and another chess-like design 50S2 with square side length 250 nm against 500 nm for 50S. The results in Fig. 9 show that the temperature variation during unloading is -8.07 K for 50H2 and -5.68 K for 50S2, which are very close to the 50H and 50S, respectively. The main difference comes from the input energy (hysteresis loop) that diminishes as the intermetallic particles are refined. Therefore, the COP of 50H2 is 71.05 against 67.13 for 50H, while the COP of 50CS2 is 47.94 against 29.22 for 50S. This means that the COP of the material can be boosted without noticeable degradation of the temperature variation only by decreasing the aspect ratio of the intermetallic phase for constant volume fraction. These quantitative results are explained by the evolution of the martensite phase and local temperature distribution in the inset of Fig. 9. The higher COP enhancement in the “chess design” finds its root in the sharp vertices acting as ideal nucleation site for martensitic phase transformation. Therefore, by decreasing the aspect ratio, the transformation becomes easier in 50S2 due to the higher number of initiation sites. In addition, the increase of vertex number generates stiffer behavior which decreases the hysteresis loop size, thus improve the COP.

The quantitative results for all the studied cases are summarized in Table 3 that gives the input energy, maximum average temperature variation after unloading, and COP.

Table 3

Summary of the eCE simulation results.

Specimen	Input energy (MJ)	Unloading ΔT (K)	COP
BM	2.743	-16.86	12.92
50H Ti ₂ Ni	1.436	-8.15	67.13
50H Ni ₄ Ti ₃	1.303	-8.17	14.29
50H Ni ₃ Ti	1.304	-8.07	16.18
35H Ti ₂ Ni	1.707	-10.7	56.31
65H Ti ₂ Ni	1.021	-5.55	79.94
50 V Ti ₂ Ni	0.682	-2.32	43.75
50D Ti ₂ Ni	1.642	-6.03	27.32
50C Ti ₂ Ni	1.283	-4.21	40.06
50H2 Ti ₂ Ni	1.343	-8.07	71.05
50S Ti ₂ Ni	2.353	-5.73	29.22
50S2 Ti ₂ Ni	1.422	-5.68	47.94

4. Conclusion

Materials for solid-state cooling require a sufficient temperature change caused by a reversible phase transformation, at the same time a high enough coefficient of performance (COP) to minimize the required energy for phase transformation. Unlike the conventional practice in the SMA field that suggests avoid formation of nonequiatomic brittle phases, in this work, we created microarchitectures by different combinations of matrix and intermetallic phases. We conducted a phase-field study to understand how various microscale features of the matrix and intermetallic phases can affect the eCE of NiTi microcomposites. To this end, we designed NiTi-based elastocaloric SMA composite material

with the highest hitherto reported material's eCE efficiency resulting from their intricate and distinct matrix and intermetallic phases. For an applied maximum compressive stress of 1200 MPa at room temperature, Ti₂Ni intermetallic with very high heat capacity displays a COP that is four times higher than those with Ni₄Ti₃ and Ni₃Ti. An increase of the content of Ti₂Ni intermetallic decreases the average temperature variation due to the lower existence of transformable material but boosts the COP of the micro-composite. Simulations of various microcomposites with different intermetallic geometries showed different mechanical and eCE responses can be tailored by changing the orientation of intermetallic strips or using more complex designs. All the cases showed a high COP for Ti₂Ni intermetallic phase. By decreasing the size of the intermetallic strips/particles, the COP was improved without any loss of the maximum average temperature variation. Our findings demonstrate that by controlling the nano and micro-scale features, materials with superior eCE can be obtained for the development of next generation solid-state cooling devices. In summary, it is desired to generate intermetallic phases with high modulus (for low input energy), very high thermal conductivity (for the temperature), and a very high heat capacity (for the output energy).

Declaration of Competing Interest

The authors declare that they have no known competing financial interests or personal relationships that could have appeared to influence the work reported in this paper.

Acknowledgement

This work was supported by the U.S. Department of Energy, Office of Science, Basic Energy Sciences, under Award number DE-SC0019279. The authors are grateful for the computer time allocation provided by the Extreme Science and Engineering Discovery Environment (XSEDE) to complete the simulations.

Data Availability

The datasets generated and/or analyzed in this study are available from the corresponding author on reasonable request.

References

- J.M. Jani, M. Leary, A. Subic, M.A. Gibson, A review of shape memory alloy research, applications and opportunities, *Materials & Design* (1980-2015) 56 (2014) 1078-1113.
- D.J. Hartl, D.C. Lagoudas, Aerospace applications of shape memory alloys, *Proceedings of the Institution of Mechanical Engineers, Part G: Journal of Aerospace Engineering* 221 (4) (2007) 535-552.
- M. Es-Souni, M. Es-Souni, H. Fischer-Brandies, Assessing the biocompatibility of NiTi shape memory alloys used for medical applications, *Analytical and bioanalytical chemistry* 381 (3) (2005) 557-567.
- A. Cladera, B. Weber, C. Leinenbach, C. Czaderski, M. Shahverdi, M. Motavalli, Iron-based shape memory alloys for civil engineering structures: An overview, *Construction and building materials* 63 (2014) 281-293.
- C. Cissé, W. Zaki, T. Ben Zineb, Numerical simulation of the behavior of steel T-stubs connected by Fe-based shape memory alloy bolts, *Journal of Intelligent Material Systems and Structures* 29 (16) (2018) 3284-3292.
- C. Cissé, W. Zaki, T.B. Zineb, Finite element analysis of a 3D Fe-based SMA cellular beam with highly heterogeneous stress and strain distributions, *Behavior and Mechanics of Multifunctional Materials and Composites 2017*, International Society for Optics and Photonics, 2017, p. 101650E.
- C. Cissé, W. Zaki, T.B. Zineb, A review of constitutive models and modeling techniques for shape memory alloys, *International Journal of Plasticity* 76 (2016) 244-284.
- C. Cissé, W. Zaki, T.B. Zineb, A review of modeling techniques for advanced effects in shape memory alloy behavior, *Smart Materials and Structures* 25 (10) (2016) 103001.
- S. Qian, Y. Geng, Y. Wang, J. Ling, Y. Hwang, R. Radermacher, I. Takeuchi, J. Cui, A review of elastocaloric cooling: Materials, cycles and system integrations, *International journal of refrigeration* 64 (2016) 1-19.
- A. Chauhan, S. Patel, R. Vaish, C.R. Bowen, A review and analysis of the elastocaloric effect for solid-state refrigeration devices: Challenges and opportunities, *MRS Energy & Sustainability* 2 (2015).
- H. Sehitoglu, Y. Wu, E. Ertekin, Elastocaloric effects in the extreme, *Scripta Materialia* 148 (2018) 122-126.
- G.J. Pataky, E. Ertekin, H. Sehitoglu, Elastocaloric cooling potential of NiTi, Ni₂FeGa, and CoNiAl, *Acta Materialia* 96 (2015) 420-427.
- W. Goetzler, R. Zogg, J. Young, C. Johnson, Energy savings potential and RD&D opportunities for non-vapor-compression HVAC technologies, Navigant Consulting Inc., prepared for US Department of Energy (2014).
- X. Moya, S. Kar-Narayan, N.D. Mathur, Caloric materials near ferroic phase transitions, *Nature materials* 13 (5) (2014) 439-450.
- L. Mañosa, A. Planes, M. Acet, Advanced materials for solid-state refrigeration, *Journal of Materials Chemistry A* 1 (16) (2013) 4925-4936.
- S. Fähler, U.K. Rößler, O. Kastner, J. Eckert, G. Eggeler, H. Emmerich, P. Entel, S. Müller, E. Quandt, K. Albe, Caloric effects in ferroic materials: new concepts for cooling, *Advanced Engineering Materials* 14 (1-2) (2012) 10-19.
- H. Hou, E. Simsek, T. Ma, N.S. Johnson, S. Qian, C. Cissé, D. Stasak, N. Al Hasan, L. Zhou, Y. Hwang, Fatigue-resistant high-performance elastocaloric materials made by additive manufacturing, *Science* 366 (6469) (2019) 1116-1121.
- J. Tušek, K. Engelbrecht, D. Eriksen, S. Dall'Olio, J. Tušek, N. Pryds, A regenerative elastocaloric heat pump, *Nature Energy* 1 (10) (2016) 1-6.
- K. Mukherjee, S. Sircar, N.B. Dahotre, Thermal effects associated with stress-induced martensitic transformation in a TiNi alloy, *Materials Science and Engineering* 74 (1) (1985) 75-84.
- H. Ossmer, C. Chluba, B. Krevet, E. Quandt, M. Rohde, M. Kohl, Elastocaloric cooling using shape memory alloy films, *Journal of Physics: Conference Series*, IOP Publishing (2013) 012138.
- H. Ossmer, F. Lambrecht, M. Gültig, C. Chluba, E. Quandt, M. Kohl, Evolution of temperature profiles in TiNi films for elastocaloric cooling, *Acta materialia* 81 (2014) 9-20.
- H. Ossmer, C. Chluba, M. Güeltig, E. Quandt, M. Kohl, Local evolution of the elastocaloric effect in TiNi-based films, *Shape Memory and Superelasticity* 1 (2) (2015) 142-152.
- L. Mañosa, A. Planes, Materials with giant mechanocaloric effects: cooling by strength, *Advanced Materials* 29 (11) (2017) 1603607.
- H. Ossmer, F. Wendler, M. Güeltig, F. Lambrecht, S. Miyazaki, M. Kohl, Energy-efficient miniature-scale heat pumping based on shape memory alloys, *Smart Materials and Structures* 25 (8) (2016) 085037.
- M. Schmidt, J. Ullrich, A. Wiczorek, J. Frenzel, A. Schütze, G. Eggeler, S. Seelecke, Thermal stabilization of NiTiCuV shape memory alloys: observations during elastocaloric training, *Shape Memory and Superelasticity* 1 (2) (2015) 132-141.
- S.M. Kirsch, F. Welsch, N. Michaelis, M. Schmidt, A. Wiczorek, J. Frenzel, G. Eggeler, A. Schütze, S. Seelecke, NiTi-Based Elastocaloric Cooling on the Macroscale: From Basic Concepts to Realization, *Energy Technology* 6 (8) (2018) 1567-1587.
- F. Bruederlin, H. Ossmer, F. Wendler, S. Miyazaki, M. Kohl, SMA foil-based elastocaloric cooling: from material behavior to device engineering, *Journal of Physics D: Applied Physics* 50 (42) (2017) 424003.
- M. Schmidt, S.-M. Kirsch, S. Seelecke, A. Schütze, Elastocaloric cooling: from fundamental thermodynamics to solid state air conditioning, *Science and Technology for the Built Environment* 22 (5) (2016) 475-488.
- J. Frenzel, G. Eggeler, E. Quandt, S. Seelecke, M. Kohl, High-performance elastocaloric materials for the engineering of bulk-and micro-cooling devices, *MRS Bulletin* 43 (4) (2018) 280-284.
- P. Kabirifar, A. Žerovnik, Ž. Ahčin, L. Porenta, M. Brojan, J. Tušek, Elastocaloric Cooling: State-of-the-art and Future Challenges in Designing Regenerative Elastocaloric Devices, *Strojinski Vestnik/Journal of Mechanical Engineering* 65 (2019) 615-630.
- H. Ossmer, S. Miyazaki, M. Kohl, Elastocaloric heat pumping using a shape memory alloy foil device, 2015 Transducers-2015 18th International Conference on Solid-State Sensors, Actuators and Microsystems (TRANSDUCERS), IEEE, 2015, pp. 726-729.
- G. Ulpiani, F. Bruederlin, R. Weidemann, G. Ranzi, M. Santamouris, M. Kohl, Upscaling of SMA film-based elastocaloric cooling, *Applied Thermal Engineering* 180 (2020) 115867.
- D.J. Sharar, A.C. Leff, A.A. Wilson, A. Smith, High-capacity high-power thermal energy storage using solid-solid martensitic transformations, *Applied Thermal Engineering* 187 (2021) 116490.
- C. Bechtold, C. Chluba, R. Lima de Miranda, E. Quandt, High cyclic stability of the elastocaloric effect in sputtered NiTiCu shape memory films, *Applied Physics Letters* 101 (9) (2012) 091903.
- C. Chluba, W. Ge, R.L. de Miranda, J. Strobel, L. Kienle, E. Quandt, M. Wuttig, Ultralow-fatigue shape memory alloy films, *Science* 348 (6238) (2015) 1004-1007.
- K. Engelbrecht, J. Tušek, D. Eriksen, T. Lei, C.-Y. Lee, J. Tušek, N. Pryds, A regenerative elastocaloric device: experimental results, *Journal of Physics D: Applied Physics* 50 (42) (2017) 424006.
- L. Porenta, P. Kabirifar, A. Žerovnik, M. Čebroň, B. Žužek, M. Dolenc, M. Brojan, J. Tušek, Thin-walled Ni-Ti tubes under compression: ideal candidates for efficient and fatigue-resistant elastocaloric cooling, *Applied Materials Today* 20 (2020) 100712.
- S. Qian, Y. Wang, Y. Geng, J. Ling, J. Muehlbauer, Y. Hwang, R. Radermacher, I. Takeuchi, Experimental Evaluation of Compressive Elastocaloric Cooling

- System, International Refrigeration and Air Conditioning Conference, Purdue e-Pubs, 2016.
- [39] F. Bruederlin, L. Bumke, C. Chluba, H. Ossmer, E. Quandt, M. Kohl, Elastocaloric cooling on the miniature scale: a review on materials and device engineering, *Energy Technology* 6 (8) (2018) 1588–1604.
- [40] C. Chluba, H. Ossmer, C. Zamponi, M. Kohl, E. Quandt, Ultra-low fatigue quaternary TiNi-based films for elastocaloric cooling, *Shape Memory and Superelasticity* 2 (1) (2016) 95–103.
- [41] H. Ossmer, C. Chluba, S. Kauffmann-Weiss, E. Quandt, M. Kohl, TiNi-based films for elastocaloric microcooling—fatigue life and device performance, *APL Materials* 4 (6) (2016) 064102.
- [42] J. Chen, K. Zhang, Q. Kan, H. Yin, Q. Sun, Ultra-high fatigue life of NiTi cylinders for compression-based elastocaloric cooling, *Applied Physics Letters* 115 (9) (2019) 093902.
- [43] J. Cui, Y. Wu, J. Muehlbauer, Y. Hwang, R. Radermacher, S. Fackler, M. Wuttig, I. Takeuchi, Demonstration of high efficiency elastocaloric cooling with large ΔT using NiTi wires, *Applied Physics Letters* 101 (7) (2012) 073904.
- [44] L. Mañosa, S. Jarque-Farnos, E. Vives, A. Planes, Large temperature span and giant refrigerant capacity in elastocaloric Cu-Zn-Al shape memory alloys, *Applied Physics Letters* 103 (21) (2013) 211904.
- [45] H. Wang, H. Huang, J. Xie, Effects of Strain Rate and Measuring Temperature on the Elastocaloric Cooling in a Columnar-Grained Cu71Al17.5Mn11.5 Shape Memory Alloy, *Metals* 7(12) (2017) 527.
- [46] C. Cissé, M. Asle Zaeem, On the elastocaloric effect in CuAlBe shape memory alloys: A quantitative phase-field modeling approach, *Computational Materials Science* 183 (2020) 109808.
- [47] Y. Wu, E. Ertekin, H. Sehitoglu, Elastocaloric cooling capacity of shape memory alloys—Role of deformation temperatures, mechanical cycling, stress hysteresis and inhomogeneity of transformation, *Acta Materialia* 135 (2017) 158–176.
- [48] A. Wiczorek, J. Frenzel, M. Schmidt, B. Maaß, S. Seelecke, A. Schütze, G. Eggeler, Optimizing Ni-Ti-based shape memory alloys for ferroic cooling, *Functional Materials Letters* 10 (01) (2017) 1740001.
- [49] D. Cong, W. Xiong, A. Planes, Y. Ren, L. Mañosa, P. Cao, Z. Nie, X. Sun, Z. Yang, X. Hong, Colossal elastocaloric effect in ferroelastic Ni-Mn-Ti alloys, *Physical review letters* 122 (25) (2019) 255703.
- [50] F. Wendler, H. Ossmer, C. Chluba, E. Quandt, M. Kohl, Mesoscale simulation of elastocaloric cooling in SMA films, *Acta Materialia* 136 (2017) 105–117.
- [51] J. Tušek, K. Engelbrecht, L. Mañosa, E. Vives, N. Pryds, Understanding the thermodynamic properties of the elastocaloric effect through experimentation and modelling, *Shape Memory and Superelasticity* 2 (4) (2016) 317–329.
- [52] H. Hou, E. Simsek, D. Stasak, N. Al Hasan, S. Qian, R. Ott, J. Cui, I. Takeuchi, Elastocaloric cooling of additive manufactured shape memory alloys with large latent heat, *Journal of Physics D: Applied Physics* 50 (40) (2017) 404001.
- [53] C. Ma, D. Gu, D. Dai, M. Xia, H. Chen, Selective growth of Ni₄Ti₃ precipitate variants induced by complicated cyclic stress during laser additive manufacturing of NiTi-based composites, *Materials Characterization* 143 (2018) 191–196.
- [54] P. Salvetr, J. Vavřík, A. Školáková, P. Novák, Formation of Intermetallics Layers in Ni-Ti System Prepared by Direct Energy Deposition, *Manufacturing Technology* 19 (4) (2019) 674–679.
- [55] D. Gu, C. Ma, In-situ formation of Ni₄Ti₃ precipitate and its effect on pseudoelasticity in selective laser melting additive manufactured NiTi-based composites, *Applied Surface Science* 441 (2018) 862–870.
- [56] C. Wang, X. Tan, Z. Du, S. Chandra, Z. Sun, C. Lim, S. Tor, C. Lim, C. Wong, Additive manufacturing of NiTi shape memory alloys using pre-mixed powders, *Journal of Materials Processing Technology* 271 (2019) 152–161.
- [57] M. Kaya, A. Buğutekin, N. Orhan, Effect of solution treatment on thermal conductivity of porous NiTi shape memory alloy, *International Journal of Thermophysics* 32 (3) (2011) 665–673.
- [58] B. Krevet, V. Pinneker, M. Rhode, C. Bechthold, E. Quandt, M. Kohl, Evolution of temperature profiles during stress-induced transformation in NiTi thin films, *Materials Science Forum, Trans Tech Publ*, 2013, pp. 287–291.
- [59] D. Luo, Y. Feng, P. Verma, Modeling and analysis of an integrated solid state elastocaloric heat pumping system, *Energy* 130 (2017) 500–514.
- [60] T. Hess, L. Maier, P. Corhan, O. Schäfer-Welsen, J. Wöllenstein, K. Bartholomé, Modelling cascaded caloric refrigeration systems that are based on thermal diodes or switches, *International Journal of Refrigeration* 103 (2019) 215–222.
- [61] S. Qian, L. Yuan, J. Yu, G. Yan, Numerical modeling of an active elastocaloric regenerator refrigerator with phase transformation kinetics and the matching principle for materials selection, *Energy* 141 (2017) 744–756.
- [62] S. Qian, J. Ling, Y. Hwang, R. Radermacher, I. Takeuchi, Thermodynamics cycle analysis and numerical modeling of thermoelastic cooling systems, *International Journal of Refrigeration* 56 (2015) 65–80.
- [63] S. Qian, A. Alabdulkarem, J. Ling, J. Muehlbauer, Y. Hwang, R. Radermacher, I. Takeuchi, Performance enhancement of a compressive thermoelastic cooling system using multi-objective optimization and novel designs, *International Journal of Refrigeration* 57 (2015) 62–76.
- [64] M. Maraldi, L. Molari, D. Grandi, A non-isothermal phase-field model for shape memory alloys: Numerical simulations of superelasticity and shape memory effect under stress-controlled conditions, *Journal of intelligent material systems and structures* 23 (10) (2012) 1083–1092.
- [65] D. Grandi, M. Maraldi, L. Molari, A macroscale phase-field model for shape memory alloys with non-isothermal effects: Influence of strain rate and environmental conditions on the mechanical response, *Acta Materialia* 60 (1) (2012) 179–191.
- [66] R. Dhote, M. Fabrizio, R. Melnik, J. Zu, Hysteresis phenomena in shape memory alloys by non-isothermal Ginzburg-Landau models, *Communications in Nonlinear Science and Numerical Simulation* 18 (9) (2013) 2549–2561.
- [67] R.P. Dhote, H. Gomez, R.N. Melnik, J. Zu, Shape memory alloy nanostructures with coupled dynamic thermo-mechanical effects, *Computer Physics Communications* 192 (2015) 48–53.
- [68] M. Mamivand, M. Asle Zaeem, H. El Kadiri, A review on phase field modeling of martensitic phase transformation, *Computational Materials Science* 77 (2013) 304–311.
- [69] L.D. Landau, Collected papers of LD Landau, Pergamon, 1965.
- [70] C. Cissé, M. Asle Zaeem, An Asymmetric Elasto-Plastic Phase-Field Model for Shape Memory Effect, Pseudoelasticity and Thermomechanical Training in Polycrystalline Shape Memory Alloys, *Acta Materialia* 201 (2020) 580–595.
- [71] C. Cissé, M. Asle Zaeem, A Phase-Field Model for Non-Isothermal Phase Transformation and Plasticity in Polycrystalline Yttria-Stabilized Tetragonal Zirconia, *Acta Materialia* 191 (2020) 111–123.
- [72] K. Knowles, D. Smith, The crystallography of the martensitic transformation in equiatomic nickel-titanium, *Acta Metallurgica* 29 (1) (1981) 101–110.
- [73] K.F. Hane, T.W. Shield, Microstructure in the cubic to monoclinic transition in titanium-nickel shape memory alloys, *Acta materialia* 47 (9) (1999) 2603–2617.
- [74] S.M. Allen, J.W. Cahn, A microscopic theory for antiphase boundary motion and its application to antiphase domain coarsening, *Acta metallurgica* 27 (6) (1979) 1085–1095.
- [75] L.D. Landau, LD Landau, Pergamon Press, 1965.
- [76] M. Ataei, A. Zarei-Hanzaki, A. Shamsolhodaei, Shape memory response and mechanical properties of warm deformed NiTi intermetallic alloy, *Materials Science and Engineering: A* 680 (2017) 291–296.
- [77] X. Li, Y. Su, A phase-field study of the martensitic detwinning in NiTi shape memory alloys under tension or compression, *Acta Mechanica* 231 (4) (2020) 1539–1557.
- [78] R. Hamilton, H. Sehitoglu, Y. Chumlyakov, H. Maier, Stress dependence of the hysteresis in single crystal NiTi alloys, *Acta Materialia* 52 (11) (2004) 3383–3402.
- [79] P. Šittner, L. Heller, J. Pilch, C. Curfs, T. Alonso, D. Favier, Young's modulus of austenite and martensite phases in superelastic NiTi wires, *Journal of materials engineering and performance* 23 (7) (2014) 2303–2314.
- [80] N. Sharma, Current activated tip sintering of Ni-Ti intermetallics, San Diego State University, 2014.
- [81] M.F.-X. Wagner, W. Windl, Elastic anisotropy of Ni₄Ti₃ from first principles, *Scripta Materialia* 60 (4) (2009) 207–210.
- [82] Q. Chen, Z. Huang, Z. Zhao, C. Hu, First-principles study on the structural, elastic, and thermodynamics properties of Ni₃X (X: Al, Mo, Ti, Pt, Si, Nb, V, and Zr) intermetallic compounds, *Applied Physics A* 116 (3) (2014) 1161–1172.
- [83] D. Toprek, J. Belosevic-Cavor, V. Koteski, Ab initio studies of the structural, elastic, electronic and thermal properties of NiTi₂ intermetallic, *Journal of Physics and Chemistry of Solids* 85 (2015) 197–205.
- [84] P. Villars, K. Cenzual, H. Okamoto, F. Hulliger, S. Iwata, PAULING FILE Multinaries Edition—2012, Springer Materials, 2012.
- [85] Y. Terada, Thermophysical Properties of L1₂ Intermetallic Compounds of Iridium, *Platinum Metals Review* 52 (4) (2008) 208–214.
- [86] A. Karati, M. Nagini, S. Ghosh, R. Shabadi, K. Pradeep, R.C. Mallik, B. Murty, U. Varadaraju, Ti₂NiCoSnSb—a new half-Heusler type high-entropy alloy showing simultaneous increase in Seebeck coefficient and electrical conductivity for thermoelectric applications, *Scientific reports* 9 (1) (2019) 1–12.
- [87] B. Onderka, A. Sypień, A. Wierzbicka-Miernik, T. Czeppe, L. Zabdyr, Heat Capacities of Some Binary Intermetallic Compounds in Al-Fe-Ni-Ti System, *Archives of Metallurgy and Materials* 55 (2) (2010) 435–439.